Check for updates

NANO · MICRO small
www.small-journal.com

Scaling and Confinement in Ultrathin Chalcogenide Films as Exemplified by GeTe

Peter Kerres, Yiming Zhou, Hetal Vaishnav, Mohit Raghuwanshi, Jiangjing Wang, Maria Häser, Marc Pohlmann, Yudong Cheng, Carl-Friedrich Schön, Thomas Jansen, Christophe Bellin, Daniel E. Bürgler, Abdur Rehman Jalil, Christoph Ringkamp, Hugo Kowalczyk, Claus M. Schneider, Abhay Shukla, and Matthias Wuttig**

Chalcogenides such as GeTe, PbTe, Sb_2Te_3, and Bi_2Se_3 are characterized by an unconventional combination of properties enabling a plethora of applications ranging from thermo-electrics to phase change materials, topological insulators, and photonic switches. Chalcogenides possess pronounced optical absorption, relatively low effective masses, reasonably high electron mobilities, soft bonds, large bond polarizabilities, and low thermal conductivities. These remarkable characteristics are linked to an unconventional bonding mechanism characterized by a competition between electron delocalization and electron localization. Confinement, that is, the reduction of the sample dimension as realized in thin films should alter this competition and modify chemical bonds and the resulting properties. Here, pronounced changes of optical and vibrational properties are demonstrated for crystalline films of GeTe, while amorphous films of GeTe show no similar thickness dependence. For crystalline films, this thickness dependence persists up to remarkably large thicknesses above 15 nm. X-ray diffraction and accompanying simulations employing density functional theory relate these changes to thickness dependent structural (Peierls) distortions, due to an increased electron localization between adjacent atoms upon reducing the film thickness. A thickness dependence and hence potential to modify film properties for all chalcogenide films with a similar bonding mechanism is expected.

1. Introduction

Chalcogenides offer a combination of properties that enables a wide range of applications. Many of them can be rapidly and reversibly switched between the amorphous and crystalline state, which frequently possess strikingly different optical and electrical properties. This property portfolio is attractive for applications as photonic switches, rewritable optical and electronic data storage and neuromorphic computing.[1] They are also characterized by moderately high electronic, yet rather low thermal conductivities, which renders them potential thermoelectrics.[2–4] Sesquichalcogenides such as Sb_2Te_3 and Bi_2Se_3 provide an electronic structure, which can be utilized in topological insulators.[5] For all of these applications it is highly desirable to tailor the material properties to meet specific requirements. Usually, this is accomplished by modifications of stoichiometry, including doping or control of the nanostructure. Yet, several recent

P. Kerres, Y. Zhou, H. Vaishnav, M. Raghuwanshi, J. Wang, M. Häser, M. Pohlmann, Y. Cheng, C.-F. Schön
I. Institute of Physics (IA)
RWTH Aachen University
52056 Aachen, Germany
E-mail: kerres@physik.rwth-aachen.de

H. Vaishnav, M. Raghuwanshi, M. Wuttig
Peter Grünberg Institute—JARA-Institute Energy-Efficient Information Technology (PGI-10)
Forschungszentrum Jülich GmbH
52428 Jülich, Germany
E-mail: wuttig@physik.rwth-aachen.de

The ORCID identification number(s) for the author(s) of this article can be found under https://doi.org/10.1002/smll.202201753.

© 2022 The Authors. Small published by Wiley-VCH GmbH. This is an open access article under the terms of the Creative Commons Attribution-NonCommercial License, which permits use, distribution and reproduction in any medium, provided the original work is properly cited and is not used for commercial purposes.

DOI: 10.1002/smll.202201753

J. Wang, Y. Cheng
Center for Alloy Innovation and Design
Key Laboratory for Mechanical Behavior of Materials
Xi'an Jiaotong University
Xi'an 710049, China

T. Jansen, D. E. Bürgler, C. M. Schneider
Peter Grünberg Institute—Electronic Properties (PGI-6)
Forschungszentrum Jülich GmbH
52428 Jülich, Germany

C. Bellin, H. Kowalczyk, A. Shukla
Institut de Minéralogie
de Physique des Matériaux et de Cosmochimie
Sorbonne Université
UMR CNRS 7590
MNHN
Paris F-75005, France

A. R. Jalil, C. Ringkamp
Peter Grünberg Institute—Semiconductor Nanoelectronics (PGI-6)
Forschungszentrum Jülich GmbH
52428 Jülich, Germany

studies have also provided some evidence for an interesting dependence of material properties on film thickness in chalcogenides. This can either provide technological challenges or interesting design opportunities. For instance, scaling the device dimensions down to the nanoscale leads to a potential challenge for phase change materials (PCM) in storage media. If small amorphous bits recrystallize spontaneously or cannot be switched at all, this creates a possible limit for further downscaling. Indeed, a number of studies have already demonstrated that phase change materials possess thickness dependent crystallization kinetics.[6–9] Remarkably, however, it has been shown that the crystallization temperature of PCMs frequently increases for ultrathin films. The amorphous phase of Sb in ultrathin films, for example, is stabilized and can be switched at room temperature, whereas thicker films already crystallize spontaneously.[4,5]

Thickness dependent opto-electronic properties are another potential opportunity upon reducing the material dimensions besides tailoring the switching kinetics. For the band gap of thin films of semiconductors, for example, a correction to the band gap E_G exists. This correction, which results from a quantization of available states in confined structures, usually scales with $\Delta E_G \propto L^{-2}$, where L is the film thickness.[10] For crystalline phase change materials, other thickness dependent material properties are also reported such as phonon frequencies, which depend on film thickness.[11–13] Also, for spintronic and thermoelectric applications, property changes with thickness are reported in topologically insulating Bismuth chalcogenides.[14–20] Yet, we are not aware of studies which compare the thickness dependence of physical properties for the two different solid states of chalcogenide materials. Could it be that there is a difference in the thickness dependence of material properties for a given compound in its amorphous and crystalline phase? For ordinary semiconductors, such a difference is not expected and has never been observed to our knowledge. Yet, most phase change materials alter their bonding mechanism upon crystallization from ordinary covalent to metavalent bonding.[21] Theoretical work has already predicted a distinctly different thickness dependence of the properties of covalent and metavalent chalcogenides.[22] Hence, one can wonder if phase change materials possibly reveal a different thickness dependence of their opto-electronic properties in their two different solid states? Answering this question and discussing the implications of the surprising answer is the goal of this manuscript. To characterize ultrathin films with well-defined properties, the films need to be ultra-smooth, dense, contamination-free and, for the crystalline films, possess a well-defined texture. The crystalline films presented here are thus grown by Molecular Beam epitaxy. Subsequently, they are capped with a protective Al_2O_3 layer without breaking the vacuum. The amorphous films are grown with sputter deposition at room temperature to ensure a layer which is as dense as possible. They are capped with a protective $(ZnS)_{80}(SiO_2)_{20}$ layer without breaking the vacuum.

C. M. Schneider, M. Wuttig
JARA-FIT
RWTH Aachen University
52056 Aachen, Germany

2. Results

2.1. Thickness Dependence of the Optical Properties of Amorphous and Crystalline GeTe

For many semiconductors, confinement effects have been reported. This confinement leads to a thickness dependence of the energy of electronic states in the vicinity of the Fermi level. Since these states govern the optical properties of a semiconductor, we expect a thickness dependence of the dielectric function in the infrared and visible range if confinement effects are prevalent. Therefore, spectroscopic ellipsometry with wave lengths between 240 and 1720 nm has been utilized to determine the dielectric function of amorphous and crystalline GeTe films of different thicknesses. **Figure 1**a,b shows the dielectric function of amorphous films with increasing thickness. The dielectric function hardly changes upon increasing film thickness from 5 to 90 nm. Only a marginal redshift of the absorption maximum is observed upon a tenfold increase of film thickness.

For the crystalline films, on the contrary, a pronounced thickness dependence of the dielectric function is observed as shown in Figure 1c,d. Furthermore, there are striking differences in the dielectric function of amorphous and crystalline films. The pronounced difference of the dielectric function between amorphous and crystalline phase change materials is one of the trademarks of these materials, which is well-known. It is surprising, however, that this difference is thickness dependent. We are not aware of any previous study of the thickness dependence of this difference. Compared to amorphous GeTe films, all crystalline samples show a Drude feature, that is, evidence for free charge carriers at low energies and a stronger optical absorption. With increasing film thickness, the peak in the optical absorption, that is, ε_2 increases and shifts to lower energies. The increase in the peak height is strongest below 10 nm but is still visible up to 20 nm. This trend is also shown in **Figure 2**, where the maximum value of ε_2 is plotted. This maximum decreases with decreasing film thickness towards the value for the amorphous films, while the amorphous samples possess a rather constant value of the maximum of ε_2. Confinement effects are hence pronounced for crystalline films of GeTe, while no obvious effects are observed for amorphous GeTe films. In the following, other relevant film properties are explored to find a possible explanation for this striking difference.

2.2. Thickness Dependence of the Vibrational Properties of Amorphous and Crystalline GeTe

To determine the vibrational properties as a function of film thickness, Raman measurements have been employed. Several previous studies have already reported on the thickness dependence of the Raman spectra of crystalline GeTe films, which are governed by an E and an A_1 mode, at around 80 and 120 cm^{-1}, respectively.[23] The Raman measurements in **Figure 3**a show these two modes. The data shown resemble previous measurements.[11,12,24] The absence of an oxide related mode at 140 cm^{-1} implies that oxidation does not even affect the thinner GeTe films.[25] All studies, including the new data presented here, agree that crystalline GeTe films have a pronounced thickness dependence of their mode frequencies, shown in

© 2022 The Authors. Small published by Wiley-VCH GmbH

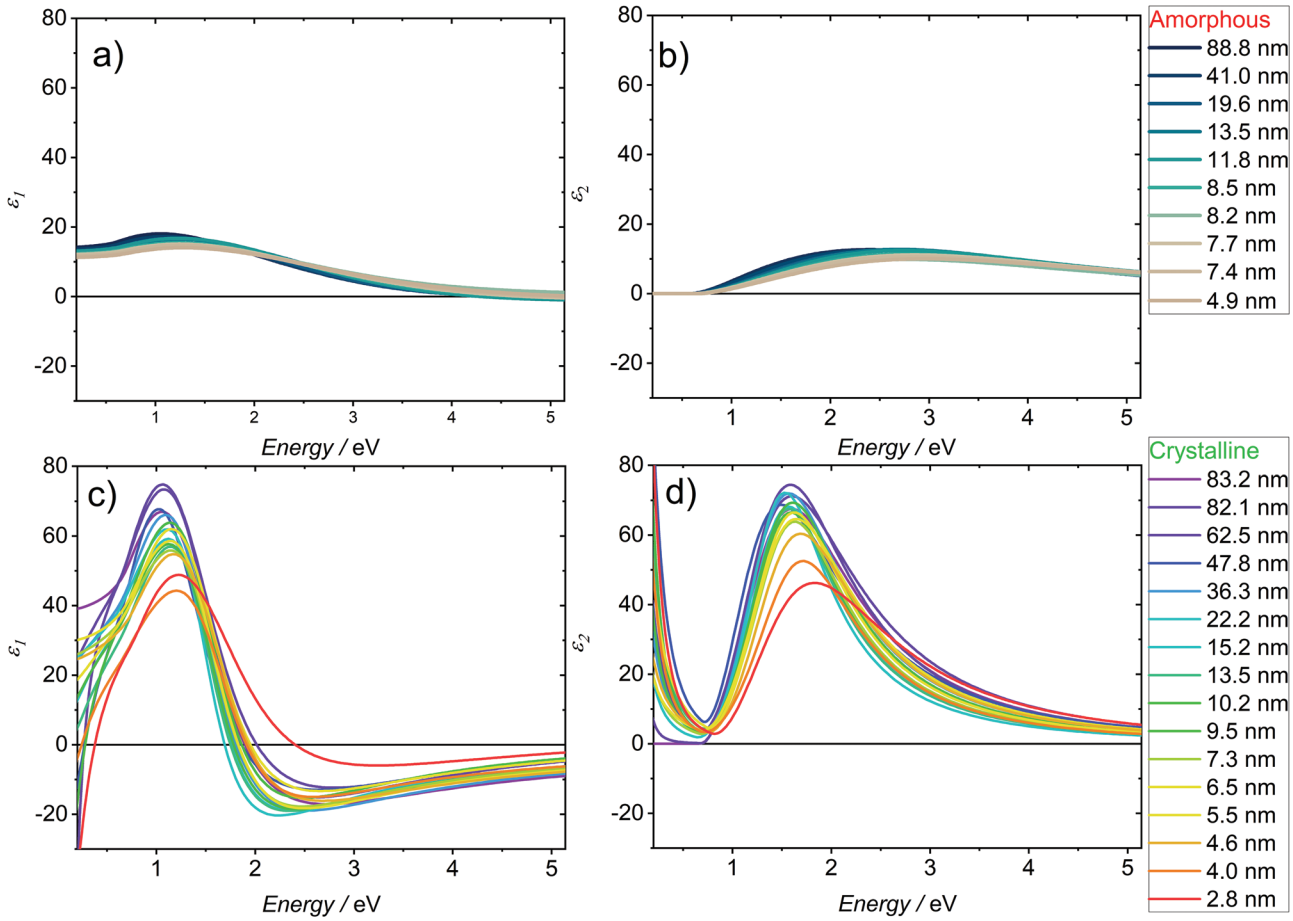

Figure 1. Dielectric function of amorphous and crystalline GeTe thin films for different film thicknesses: a) real part and b) imaginary part of the dielectric function of the amorphous samples, c) real part and d) imaginary part of the dielectric function of the crystalline samples, which are stronger and have an increased thickness dependence.

Figure 3b. It is striking to see that the vibrational frequency of both modes decreases significantly with increasing film thickness, even though the average number of neighboring atoms increases with film thickness. This is a rather unusual thickness dependence. The amorphous films feature a broad Bose Peak at low wavenumbers and have significantly higher phonon frequencies at roughly 120 and 155 cm^{-1} compared to the crystalline modes. Given the broadness of the amorphous features, the data matches the previously reported modes around 125 and 162 cm^{-1}.[26] Possibly more striking, while the modes of the crystalline phase show a pronounced thickness dependence, this is not the case for the amorphous films. With decreasing film thickness, the frequencies of the crystalline film approach those of the amorphous films. Hence, both for the vibrational and the optical properties there is a recurrent pattern. There is a tremendous difference in confinement effects for the amorphous and the crystalline phases. The properties of the crystalline films approach those of the amorphous samples with decreasing thickness. These observations demand an explanation.

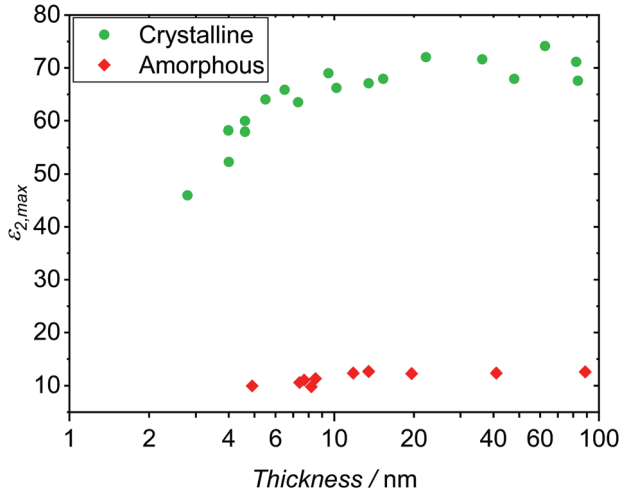

Figure 2. Maximum value of ε_2 as a function of thickness for the amorphous (red) and crystalline (green) samples shows the increased thickness dependence for the crystalline samples.

2.3. Thickness Dependence of the Atomic Arrangement in Crystalline GeTe

The pronounced thickness dependence of the vibrational modes and optical properties of crystalline GeTe thin films is possibly related to a thickness dependence of the atomic arrangement.

© 2022 The Authors. Small published by Wiley-VCH GmbH

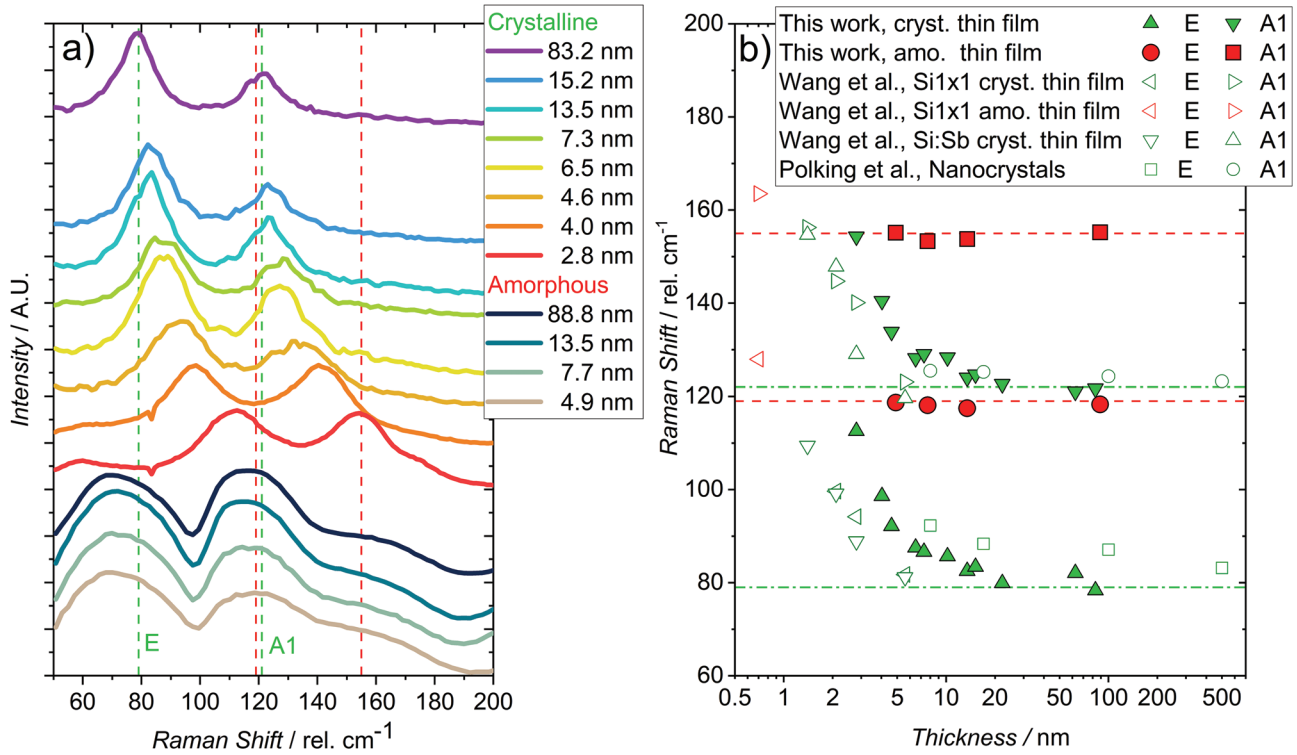

Figure 3. Raman measurements of selected crystalline and amorphous thin films. a) Spectrum in the range of the A1 and E modes of GeTe, vertically offset to show the (lack of) thickness dependent evolution. The intensity was scaled so that the modes are equally visible in the films. b) Thickness dependent shifts of the GeTe modes in the amorphous (red symbols) and crystalline (green symbols) phase, plotted together with already published data of Wang et al.[11,12] for thin films on two different Si substrates and Polking et al.[24] for nanocrystals. While the frequencies of the amorphous samples are independent of the thickness, the modes are strengthened for ultrathin crystalline GeTe films.

Hence, x-ray diffraction (XRD) has been used to characterize the films. The structure of crystalline GeTe can be described by the rhombohedral R3m unit cell in Figure 3c. The Miller Bravais Notation (hkil) is used to identify the lattice planes. The atomic arrangement can be understood as a small distortion of a perfect octahedral structure, characterized by 6 nearest neighbors, to an arrangement with 3 longer and 3 shorter bonds, often described as a "Peierls Distortion."[27] The same concept can also be used to describe the short range order in amorphous and liquid GeTe.[28,29] In **Figure 4** θ–2θ scans, which probe the out of plane direction, are shown of all samples. Only (0003n) GeTe reflections can be seen apart from the substrate peaks, indicative of highly textured crystalline films. Laue fringes around the lattice peaks are obtained for all samples for the (0003) and (0006) peaks, visible for the thicker films in the close ups of the (0003n) peaks in Figure 3b–d. Thus, coherently scattering epilayers of GeTe are formed in all samples. The (0003n) peaks broaden due to the finite film thickness and gradually shift towards lower values in Q-space and thus higher lattice constants for ultrathin films. **Figure 5** shows cuts through the $(1\bar{1}00)$ reflexes of selected samples for the in plane direction for a fixed tilt angle ψ, and reciprocal space maps of the $(10\bar{1}7)$ peaks, which have both an in- and out-of-plane component, at a fixed rotation angle ϕ. The in plane lattice constant observed from the $Q_{\parallel}$ position of the $(1\bar{1}00)$ peaks decreases the ultrathin films. The width of the $(1\bar{1}00)$ peaks with respect to the sample rotation does not change significantly, indicating that we preserve a biaxial texture throughout the films. The position and widths of the $(10\bar{1}7)$ peaks show the same behavior of an increasing $Q_{\parallel}$ and decreasing Q_z for the ultrathin films. The evaluation of the in plane (a) and out of plane (c) lattice parameters from the shown XRD is shown in **Figure 6** and compared with the value for the in plane lattice constant measured with reflection high energy diffraction (RHEED) during growth and values based on DFT calculation of freestanding GeTe slabs from Wang et al.[11] For both in plane and out of plane lattice parameters, the change in lattice parameter is most pronounced below 7 nm but with minor changes visible in an intermediate region. As the data density in between the bulk like samples and the region below 10 nm is comparatively low, we refrain from pinpointing the limits of changing atomic arrangement with film thickness to a certain value from XRD. A change in the in plane lattice constant is also visible during growth from the shift of the reflex position on the RHEED. The in situ lattice constant for the growth is calibrated by the substrate peak positions before growth. Below 2 nm, the films are in the blackout region, that is, have an amorphous structure.[11] Above 2 nm film thickness, the in plane lattice constant increases towards the bulk value. The fact that the same trends are observed by RHEED during deposition and by XRD after deposition indicates that the distortion is already formed during deposition and is thus an inherent film property. A comparison of the lattice constants extracted from RHEED for different samples suggests that the intermediate region extends to 15–20 nm, as shown in Figure S5, Supporting Information. This is a remarkably large range of film thicknesses, over which the atomic arrangement changes.

© 2022 The Authors. Small published by Wiley-VCH GmbH

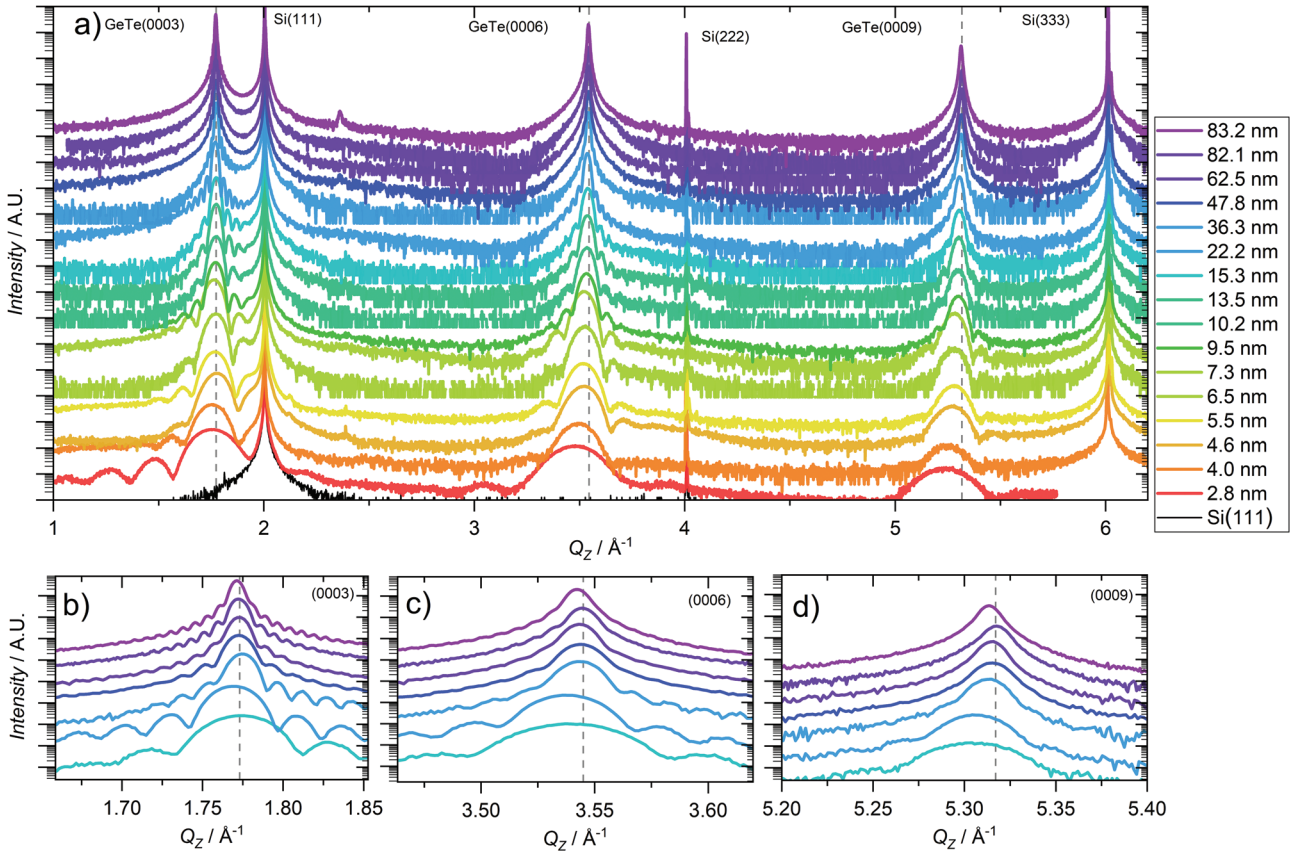

Figure 4. X-ray diffraction measurements of crystalline GeTe films for different thicknesses: a) $\theta - 2\theta$ measurements of the films, which are textured in (0001) direction and show Laue fringes besides the main diffraction peaks. The (0003n) peaks show a thickness dependent distortion towards lower Bragg angles and a larger out of plane lattice constant in ultrathin films. b–d) close ups of the (0003n) peaks for the thicker films.

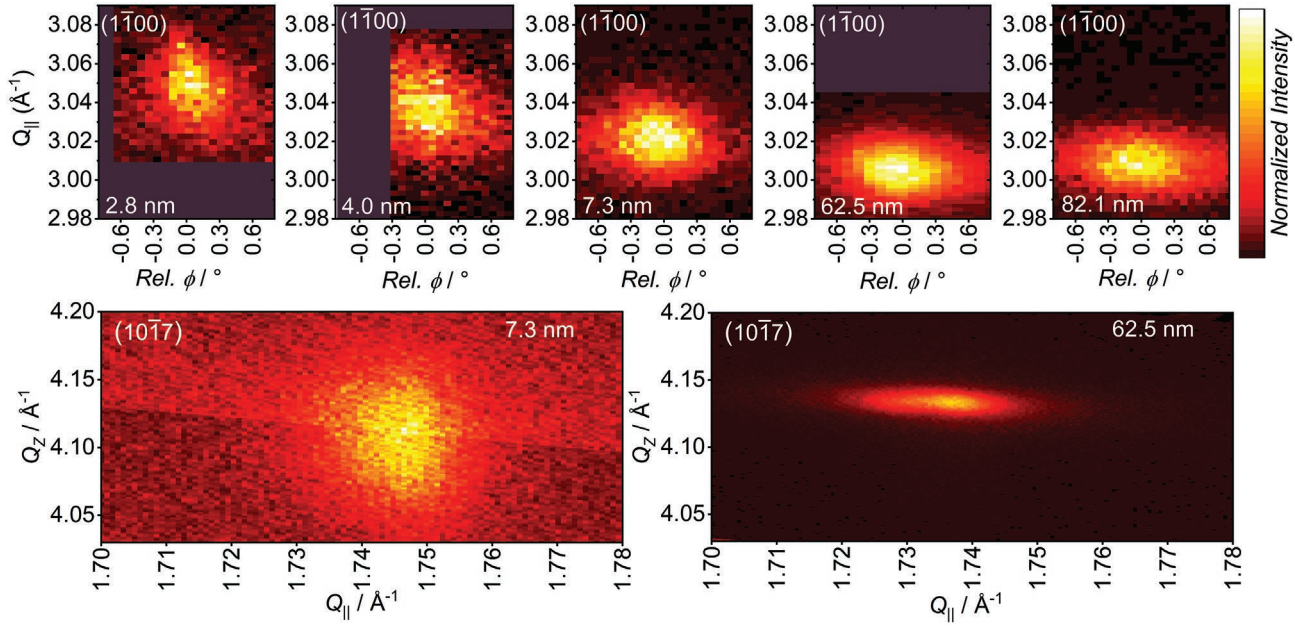

Figure 5. In plane reciprocal space maps of the $(1\bar{1}00)$ peaks (top) and reciprocal space maps of the $(10\bar{1}7)$ Peak (bottom) for different reveal a distortion towards higher Bragg angles and a lower in plane lattice constant in ultrathin films. The out of plane component of the $(10\bar{1}7)$ seconds the trend of the $\theta - 2\theta$ measurements.

© 2022 The Authors. Small published by Wiley-VCH GmbH

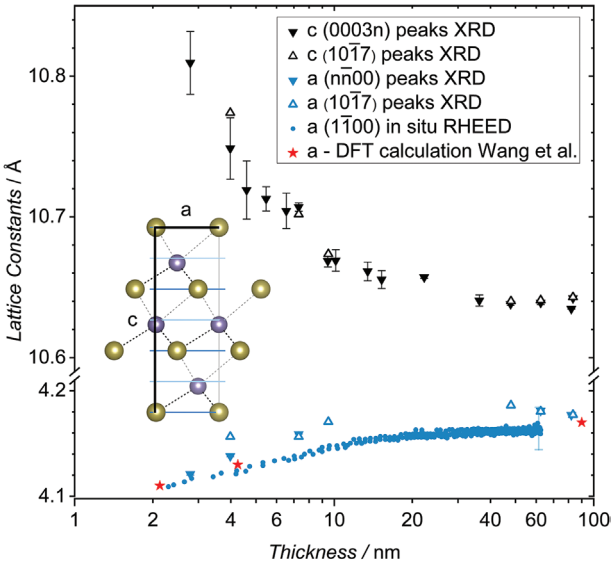

Figure 6. a In plane and c out of plane lattice constants obtained as function of film thickness. Closed triangles are calculated from peaks with either h,k,l = 0 and open triangles from the reciprocal space maps of the (10$\bar{1}$7) Peaks. Closed points depict the lattice parameter obtained from the RHEED measurement during growth of the 62.5 nm sample. Red stars are in plane lattice parameters from simulated freestanding GeTe films from Wang et al.[11] All methods agree that the unit cell is distorted toward higher c and lower a for ultrathin films. Inset drawn with VESTA.[52]

From the lattice parameters, we can calculate changes in the aspect ratio of the unit cell (c/a) and the unit cell volume. While we see a relative elongation of the lattice cell to a higher aspect ratio (3%), the cell volume does not change within 1%. Since all peaks shift gradually with film thickness and no new peaks appear, the appearance of a new phase different from the bulk R3m phase is unlikely. Furthermore, DFT calculations of freestanding GeTe slabs as presented by Wang et al. show a similar behavior of the in-plane lattice constant,[11] which implies that the change is not governed by strain imposed from the substrate. For GeTe grown on the 7 × 7 reconstruction, domain matched epitaxy is observed, with a number of rotational domains rotated with respect to the orientation of the substrate, as shown in the Azimuthal RHEED pattern and the ϕ-scans in **Figure 7**. The most intense and therefore prevalent domains on the samples are rotated by roughly 7°, in accordance to previous reports of GeTe grown on 7 × 7 reconstructed Si.[30,31] The rotation of the domains with respect to the substrate mitigates the domain misfit between substrate and thin film rather than forming a pseudomorphic, heavily strained epilayer.[31,32] Accordingly the orientation angle of the domains adjusts as the in plane lattice expands during growth as seen in Figure 7b. The change of the atomic arrangement with thickness could instead be attributed to a thickness dependent Peierls distortion, characterized by a gradual decrease of the ratio of long to short bonds R_l/R_s within the unit cell.

The inset in **Figure 8**a shows the unit cell of GeTe with two different R_l/R_s, ratios. A change of the Peierls distortion in GeTe will alter the displacement of the Ge/Te sub-lattices from a cubic arrangement along the *c*-axis. In kinematic diffraction theory, the intensity I for a given diffraction peak is based on the interference of waves scattered at the atomic sites. For $R_l/R_s = 1$, the Ge and Te atoms are alternating with a distance of 1/6 c along the *c*-axis. For the diffraction on [0003] planes, the waves scattered on the different atomic species have a 180° phase shift and show destructive interference. For the [0006] planes, the phase shift is 0° and the waves interfere constructively. For $R_l/R_s \neq 1$ one sublattice is shifted, and the constructive interference is reduced. The intensity ratio $I_{(0006)}/I_{(0003)}$ is largest without Peierls distortion and decreases for larger R_l/R_s . Ge vacancies also reduce the scattering centers in one sublattice and thus can reduce the intensity ratio as well. We calculated the structure factors F_i based on structure parameters from Nonaka et al.[33] and show the relation of intensity ratio and Peierls distortion in Figure 8a. A geometric factor is added to account for the experimental setup: The measured intensity is dependent on the volume V_i probed for the different peaks. The volume ratio is dependent on the incidence angles ω_i, which affects the beam footprint on the sample. The

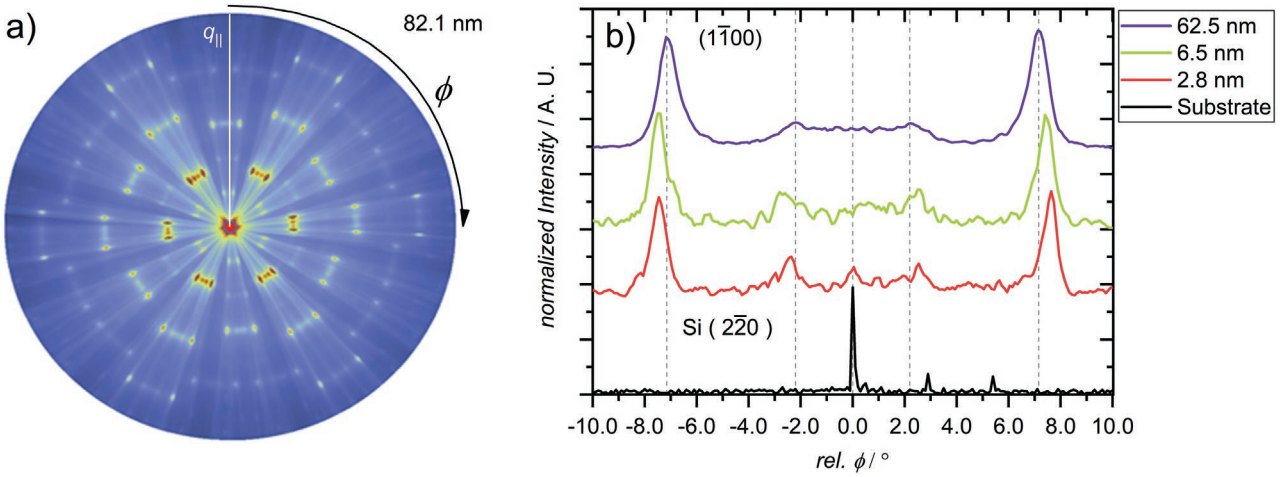

Figure 7. a) ARHEED and b) ϕ scans of films with different thicknesses. The in plane texture shows rotational domains at roughly ±2° and ±7°. The orientation angle of these domains increases slightly for thinner films.

© 2022 The Authors. Small published by Wiley-VCH GmbH

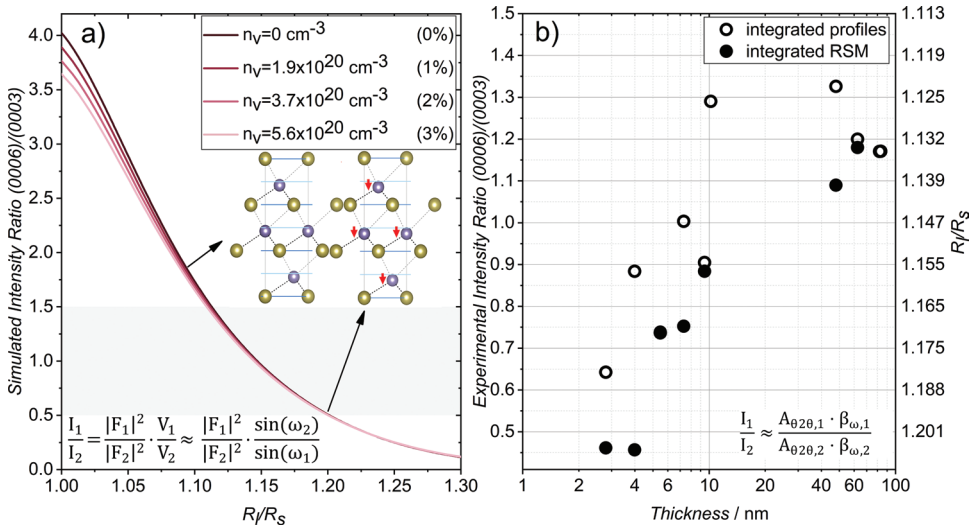

Figure 8. Calculated and experimental results for the intensity ratio of the (0003) and (0006) peaks. a) Simulated intensity ratio based on structure factor calculations for different amounts of Peierls distortion, parametrized by the R_I/R_S ratio. The structure factors are multiplied by a geometrical correction factor to account for differences in the illuminated area for both diffraction conditions. The inset shows the movement of one sublattice away from the (0006) lattice planes upon increasing Peierls distortion. Different vacancy concentrations only lead to small changes of the intensity ratio for distorted films. Hence, the observed changes of intensity ratio with film thickness in (b) can be best accounted for by changes of the Peierls distortion in GeTe films with thickness. b) Experimentally determined intensity ratio, estimated by an analysis of integrated intensities in $\theta - 2\theta$ measurements and rocking curves (circles) and direct integration of reciprocal space maps (points). Thicker films have intensity ratios between 1.1–1.3, corresponding to Peierls distortions around 1.12–1.14. For thinner films, the intensity ratio goes down to 0.6, corresponding to a distortion of around 1.18–1.20. Inset drawn with VESTA.[52]

comparison shows that for vacancy concentrations matching the reported carrier concentrations in GeTe,[34] their influence is negligible for Peierls distortions similar to or larger than the value reported for bulk GeTe (1.09).[33] We can therefore only explain the thickness dependence of the experimentally derived peak intensity ratio by a thickness dependent Peierls distortion. From the measured ratio shown in Figure 8b, we can determine the size of the Peierls distortion. These ratios were determined from integrating reciprocal space maps of both peaks (solid points) and measuring perpendicular high resolution line profiles (θ–2θ and ω–scans) and calculating the intensity ratio from the integrated area A_i of the former and the integral breath β_i of the latter. Both methods determine a decreasing intensity ratio and therefore a higher amount of Peierls distortion for the ultrathin films.

3. Discussion

3.1. Linking Changes in Atomic Arrangement to the Thickness Dependence of Optical and Vibrational Properties

The last section has shown that the thickness dependence of the optical and vibrational properties of crystalline GeTe films coincides with a thickness dependence of the atomic arrangement, and in particular a thickness dependence of the Peierls distortion. This raises the question if these two trends are closely intertwined. GeTe is characterized by an electronic structure which differs significantly from covalent semiconductors like GaAs or Si. Each atom in GeTe employs predominantly p-electrons to bond to its nearest neighbors, which are octahedrally arranged. Without any Peierls distortion, each atom hence has six nearest neighbors, with whom σ–bonds are formed from p-orbitals. For each of these six bonds, only a single electron is available, unlike in covalent bonds which require two electrons, that is, an electron pair to form this bond. The optical transitions in GeTe are thus governed by transitions between p-states.[35] These p–p transitions are dipole allowed since they are characterized by a parity change. The transition rate is described by Fermi's golden rule, which depends upon the joint density of states and the matrix element for the transition between valence band and conduction band states. This matrix element depends upon the overlap of the valence and conduction band states, which has been shown to depend upon the size of the Peierls distortion[35] and other distortions which alter the p-orbital alignment.[36] With decreasing size of the Peierls distortion, the matrix element and the maximum of the imaginary part of the dielectric function $\varepsilon_2(\omega)$ increases.[35] We demonstrate this behavior in **Figure 9**. The orbital resolved dielectric function is calculated from structures based on the XRD results and compared to the experimentally determined function. It is remarkable how well the simulated optical data fit the experiment by just considering the structural (Peierls) distortion. The optical and vibrational properties of amorphous GeTe on the contrary are rather independent of film thickness, which indicates that the atomic arrangement does not change with thickness.

3.2. Linking the Differences in Confinement Effects of Amorphous and Crystalline GeTe Films to Differences in Bonding

In the last section, the thickness dependence of the optical properties of crystalline GeTe films has been attributed to a thickness dependence of the Peierls distortion. Yet, both

© 2022 The Authors. Small published by Wiley-VCH GmbH

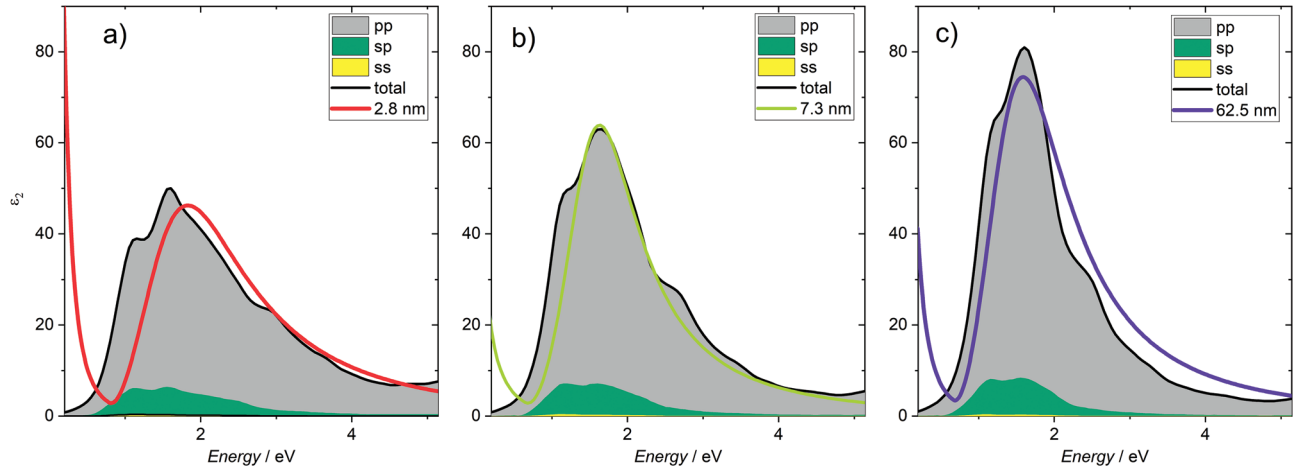

Figure 9. Imaginary part of the dielectric function ($\varepsilon_2(\omega)$) of GeTe films with increasing thickness compared with simulation results based on the experimentally determined distortion of the unit cell: a–c) Imaginary part of the dielectric function for the three different distortions, plotted together with the experimental data from Figure 1 for films of 2.8 nm (red line), 7.3 nm (green line), and 62.5 nm (purple line). The shaded areas show the contribution of s–s, s–p, and p–p transitions that make up the dielectric function, which is governed by the p–p transition. For thinner films and thus larger Peierls distortions, the overlap of the p-orbitals of adjacent atoms is reduced, which leads to a decrease of the p–p transition probability and thus a lower maximum of $\varepsilon_2(\omega)$.

amorphous and crystalline GeTe are characterized by a Peierls distortion, albeit one that differs in magnitude. Why is there no apparent change in the size of the Peierls distortion with increasing film thickness for the amorphous films? In the last few years, ample evidence has been found which points towards significant differences in bonding between many amorphous and crystalline phase change materials. Upon crystallization, materials like GeTe, Sb_2Te_3 and $GeSb_2Te_4$ show significant differences in properties such as the effective coordination number, the optical dielectric function $\varepsilon(\omega)$ and the optical dielectric constant ε_∞, a measure of the optical polarizability.[35] In addition, significant differences in the Born effective charge, a measure of the chemical bond polarizability, the electric conductivity σ or the bond rupture have been attributed to a change of bonding upon crystallization.[21] These observations can be explained best if we assume that the bonding in many crystalline chalcogenides and related compounds differs significantly from ionic, covalent, and metallic bonding, but forms a unique bonding type instead, which has been denoted as metavalent bonding. Materials that employ this bonding mechanism can be distinguished from other materials by two quantum-chemical bond descriptors, the number of electrons shared (ES) and transferred between adjacent atoms (ET), which are obtained by density functional theory (DFT) calculations.[37] This leads to a map for solids as depicted in **Figure 10**, where metavalently bonded compounds occupy a well-defined region between covalent and metallic bonding. Ordinary covalent bonds as found in Si or diamond are characterized by the formation of an electron pair between two adjacent atoms. In this case, the electrons which are responsible for the bond are localized between these neighboring atoms. One electron pair is shared between two atoms, the ES of Si is roughly 2. In solids employing metallic bonds, on the contrary, the electrons forming the bond are delocalized over several atoms, as a consequence the electrons shared value between adjacent atoms is much smaller (e.g., 0.5 for Ag). For ideal metavalent bonds, one electron (half an electron pair) is shared between neighboring atoms. In ideal cubic GeTe, the p-orbitals form chains throughout the material. The small Peierls distortion in stable GeTe decreases the p-orbital overlap and the average value of ES increases slightly as compared to the cubic state. After confining the film, the atoms adopt a more distorted structure. An increased Peierls distortion for thinner slabs of (111) oriented freestanding GeTe and GeTe was theoretically calculated by Wang et al.[11] The Peierls distortion increased from 1.11 in the bulk to 1.16 in a 6 Bilayer (≈2 nm) film, while the in plane lattice constant decreased from 4.17 to 4.11 Å.[11] For thin films of covalently bonded GaSb no similar changes of film structure with thickness have been reported.[11] For the $(01\bar{1}2)$ orientation of GeTe—which corresponds to the

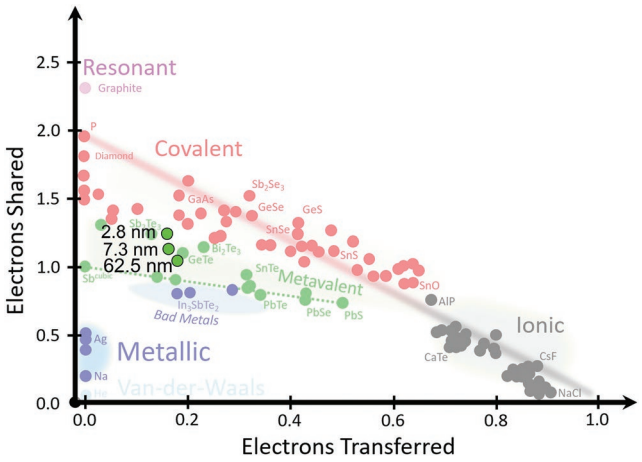

Figure 10. Map which separates different bonding mechanisms utilizing the number of electrons shared and transferred between adjacent atoms. Crystalline GeTe is found in the green region, where bonding is characterized by a competition between localization and de-localization. Redrawn with permission.[21] Copyright 2020, The Authors, Published by WILEY-VCH.

© 2022 The Authors. Small published by Wiley-VCH GmbH

(001) plane in the cubic system, more extensive theoretical studies have recently been performed by Ronneberger et al.[22] also providing ES/ET coordinates for different film thicknesses as a function of the position within the layer stack. These computations show an average increase of ES along the film normal for thinner films. A link between the Peierls distortion and ES/ET for bulk GeTe was shown by Raty et al.[38] Indeed, for the structures presented above we determine an increase of the Peierls distortion from $R_l/R_s = 1.11$ (ES = 1.05) for GeTe films with a thickness of 62 nm, to $R_l/R_s = 1.19$ (ES = 1.25) for 2.8 nm of GeTe. Upon decreasing film thickness, the metavalently bonded crystalline films thus become increasingly more covalent, since the electrons are more localized. This causes an increase of the bond strength which leads to an increase of the frequency of the vibrational modes with decreasing film thickness, as seen in the Raman spectra. The concomitant increase of the Peierls distortion leads to a reduced overlap of adjacent p-orbitals and hence a decrease of the imaginary part of the dielectric function. Thus, the change in bonding of the GeTe can explain the changes found in the Raman and spectroscopic ellipsometry measurements. In amorphous GeTe films, a broader variation of bond lengths is found because only short range order is present. Nevertheless, the average motif of short and long Bonds is similar and median values of R_l and R_s can be calculated.[29] In these amorphous films, a thickness dependence of properties is not observed. In covalent bonds the electrons are much more localized, and hence there is no competition between electron de-localization and electron localization anymore. Hence, a thickness increase cannot change the electron de-localization and the changes of film properties with thickness are much smaller, as shown in Figures 1–3. Note that the change of the vibrational modes is similar for GeTe deposited on all three different substrate terminations shown in Figure 3, even though the in plane lattice constant decreases towards the bulk value for GeTe deposited on the Sb terminated surface.[12] A similar change of the optical and vibrational modes has been reported for thin Sb films by Cheng et al.,[13] which could be explained by the proposed increase of ES for thinner films as well. The present findings reveal that the film thickness compliments the film stoichiometry as a means to tailor film properties. While we can modify the two quantum chemical bonding descriptors (ES and ET) by changes of stoichiometry, we can also increase ES by a reduction in film thickness without changing stoichiometry. This will lead to clear changes in film properties such as the optical absorption of the crystalline state ($\varepsilon_2(\omega)$), but also effective masses and hence electron mobilities as a function of thickness for GeTe films which are less than 10 nm thick. It is also plausible that this will affect the crystallization kinetics. More specifically, the increased covalence of thin GeTe films should also increase the bond strength with decreasing film thickness. This conclusion implies that thin GeTe films might require higher crystallization temperatures and should show a crystallization temperature, which increases with decreasing film thickness. This conclusion is consistent with experimental observations.[39] Yet, crystallization will also be influenced by the proximity of interfaces. Hence, considerable care has to be taken to separate the impact of heterogeneous nucleation from intrinsic changes of film properties with film thickness.

4. Conclusion

The thickness dependence of the optical and vibrational properties of amorphous and crystalline films of GeTe has been studied. While these properties show a pronounced thickness dependence for crystalline GeTe, this is not the case for the amorphous films. With decreasing film thickness, both the dielectric function and the vibrational properties of the crystalline films approach the properties of the amorphous films. Crystalline GeTe thin films show a change of atomic arrangement with film thicknesses, which can be attributed to a Peierls distortion which increases with decreasing film thickness. These changes are closely linked to changes of optical and vibrational properties with film thickness. The unconventional bonding in crystalline GeTe, that is, metavalent bonding, explains both observations. Metavalent bonding is defined by the competition between electron localization and electron delocalization. Reducing the film thickness affects this competition and increases the electron localization, making the film more covalent. For the amorphous films, on the contrary the electron localization hardly changes, as previously shown for crystalline covalently bonded films. The ability to modify the balance between localization and delocalization with film thickness in metavalently bonded materials provides ample opportunities to tailor material properties. This has been shown for GeTe in this paper and can be extended to the related metavalently bonded Sb in the work of Cheng et al.[13] Since there is a plethora of chalcogenides including GeTe, SnTe, PbTe, Sb_2Te_3, Bi_2Se_3, $Ge_2Sb_2Te_5$, and many more, which employ metavalent bonding, this promises many interesting design opportunities for phase change materials, photonic switches, thermoelectrics and topological insulators.

5. Experimental Section

Deposition: In the present study, crystalline GeTe thin films were deposited by molecular beam epitaxy (MBE) on a 3.5 × 3.5 cm^2 single side polished Si(111) substrate (N/Ph doped, 3–10 kΩ cm resistivity). RCA cleaning was performed to remove the top oxide layer and impurities from the substrate surface. As the last step of the cleaning process, the substrate was rinsed with 1% hydrofluoric acid. The substrate was immediately placed in a load lock chamber and evacuated to 10^{-8} mbar. Once this pressure was reached, the substrate was transferred to the MBE chamber, which had a base pressure of 10^{-10} to 10^{-11} mbar. The substrate was heated up to 750 °C for 30 min to achieve a 7 × 7 surface reconstruction[40] of Si(111), as shown in Figure S6a, Supporting Information. Crystalline epitaxial GeTe growth was optimized for the specific setup based on the process developed by Giussani et al.[30] The Ge and Te effusion cells were run at 1121 and 248 °C respectively, leading to a growth rate of 0.03 Å s^{-1}. The substrate heater was set to 125 °C. The growth mode was monitored in real time with in situ RHEED to ensure reproducibility. The film stoichiometry was determined with EDX for the thicker samples and did not vary by more than 1% on and within the samples. For further ex situ investigations, GeTe films were immediately and without vacuum break covered with Al_2O_3 in a dedicated oxide-MBE system with a base pressure of 4 × 10^{-10} mbar. Al_2O_3 was evaporated from an electron-beam evaporator. The deposition rate was 0.1 Å s^{-1} and the pressure raised during evaporation to 2 × 10^{-7} mbar. The sample was rotated at 6 rpm about the surface normal for a better thickness homogeneity. The amorphous GeTe films were deposited on 2 × 2 cm^2 single side polished Si(100) substrates with magnetron sputtering. The deposition was performed from a stoichiometric target at the power of

© 2022 The Authors. Small published by Wiley-VCH GmbH

20 W (DC generator) with an Ar flux of 20 sccm. To prevent oxidation, capping layers of ZnS-SiO_2 (80:20 at%) were deposited in situ from a stoichiometric target with a power of 60 W (RF generator) and an Ar flux of 20 sccm. No further heat treatment was performed on any sample.

Raman Spectroscopy: Raman measurements of the thicker crystalline films were performed using a laser wave length of 532 nm on a WITec alpha300R confocal microscope. Spectra were recorded using a 100× objective under ambient conditions. Low laser energy (0.1 mW) was used for the Raman measurements to avoid laser-induced damage of the GeTe samples, which were sensitive to light and heat. Measurements were performed on various spots to ensure representative results and the homogeneity of the sample. A resolution of around 1 cm^{-1} was achieved utilizing a grating with 1800 lines mm^{-1}. The thinner crystalline samples and the amorphous samples were measured on a Jobin-Yvon HR-460 spectrometer (1500 lines mm^{-1} grating and Andor CCD camera, spectrometer resolution being 1.5 cm^{-1}) in backscattering geometry. The primary beam was from a 514.5 nm Ar laser focused into a 2 µm spot. To obtain the mode frequencies, the Raman peaks were fitted with a series of Gaussian peaks.

X-Ray Diffraction/Reflection: XRR measurements were used to determine the thickness of the GeTe film and capping material. The out of plane texture was probed with θ–2θ scans and rocking curves. For assessment of the in plane data, ϕ-scans near the $(1\bar{1}00)$ Peaks were measured and reciprocal space maps were obtained for the $(1\bar{1}00)$ and (2200) Peaks. All X-ray experiments were performed with Cu Kα,1 radiation (1.5406 Å) on a Bruker D8 Discover. For the line profiles, the incident beam path consisted of a Goebel mirror, a 0.6 mm slit, a (220) Ge monochromator, and an automatic rotary absorber. On the detector side, a 0.6 mm slit and a LynxEye detector in 0D mode with an active area of 0.675 mm were used. For the XRR measurements, the slits were replaced by 0.1 mm slits and the detector area was adjusted accordingly. The in plane measurements were performed with a 1 mm nozzle instead of the incident slit, and an additional 2.5° axial Soller in front of the detector, with an active area of 1 mm. To obtain a grazing condition, the sample surface orientation was adjusted with two stepper motors inside the centric Eulerian cradle, and a ψ angle of 89.2° was used during the scans.

The reciprocal space maps of the $(10\bar{1}7)$ peaks were taken on a Rigaku SmartLab X-Ray Diffractometer equipped with a HyPix-3000 2D detector, which measured in the 1D mode. A Ge(220)×2 monochromator was used for the incident beam and a 5.0° Soller slit for the outgoing beam. To obtain peak positions, the line profiles were fitted with Pseudo-Voigt profiles and the reciprocal space maps with 2D Gaussian peaks. The lattice parameters were determined by linear regression where applicable.

Spectroscopy Ellipsometry: Ellipsometry spectra were measured in the spectral range from 0.72 to 5.14 eV using a J. A. Woollam M-2000UI with angles of incidence of 65°, 70°, and 75°. The light sources of the setup were deuterium and halogen lamps. A silicon charge-coupled device camera was employed for the visible and ultraviolet range detection, while an InGaAs diode array was used for the lower energy range. These detectors used in total 584 channels with an average resolution of around 7 meV. Ellipsometry spectra were recorded at room temperature.

The dielectric functions of samples were determined by establishing a 3 layer model (capping/thin film/substrate) based on matrix formalism in the CODE software. A summation of a constant dielectric background, the Tauc-Lorentz and Drude contributions was employed to describe the dielectric function of the GeTe thin films (see Figure S1, Supporting Information). The dielectric functions of capping and substrate were established on reference samples. A Downhill simplex method was used for the unconstrained optimization. All the parameters were fitted to convergence.

DFT Calculations: The electronic structure calculations were conducted using DFT (density functional theory), utilizing PAW (projector augmented wave) potentials[41] as implemented in the VASP[42–45] and ABINIT[46,47] software packages. GGA-PBE exchange-correlation functionals[48] were used for the computation. The energy cutoffs exceeded 500 eV for all calculations. A 23 × 23 × 9 k-point grids and 8 × 8 × 3 k-point grids were utilized for the calculation of the dielectric functions and the ES/ET values respectively. The dielectric functions were computed using Fermi's golden rule and a sum over states close to the Fermi level (5/14 valence/conduction states).

The DGRID code was used to calculate the electrons shared and electrons transferred values by employing Bader basins Ω,[49] defined by applying the Yu-Trinkle algorithm.[50] The initial wave function required by the DGRID software package was computed with the ABINIT software. The ES values were obtained by integration of the exchange-correlation hole over the corresponding basins. Integrating over the electrons density within a basin yields the electron population of the respective atom $N(\Omega)$. The total number of electrons transferred (TET) was then obtained by subtracting the nominal charge of the atom. To get the (relative) number of electrons transferred (ET), the TET value was further divided by the formal oxidation state of the respective atom. The ET and ES values were robust against the choice of the functional type, as these quantities mostly depended on the valence wave function.[51]

Supporting Information

Supporting Information is available from the Wiley Online Library or from the author.

Acknowledgements

This work was supported in part by the Deutsche Forschungsgemeinschaft (SFB 917) and in part by the Federal Ministry of Education and Research (BMBF, Germany) in the project NEUROTEC II (16ME0398K), M.W. furthermore acknowledges funding of a Distinguished Professorship by RWTH Aachen University. The authors acknowledge the computational resources granted from RWTH Aachen University under project RWTH0662 and the Forschungszentrum Jülich under project JARA0229. The authors also acknowledge the work of Marvin Kaminsky who helped with setting up the MBE growth process used for this work, Christoph Stampfer for access to his Raman setup, and Jean-Yves Raty for his support in the DFT calculations.

Open access funding enabled and organized by Projekt DEAL.

Conflict of Interest

The authors declare no conflict of interest.

Data Availability Statement

The data that support the findings of this study are available from the corresponding author upon reasonable request.

Keywords

metavalent bonding, molecular beam epitaxy, optical spectroscopy, Peierls distortion, X-ray diffraction

Received: March 20, 2022
Published online:

[1] P. Noe, C. Vallee, F. Hippert, F. Fillot, J.-Y. Raty, *Semicond. Sci. Technol.* **2018**, *33*, 013002.

[2] Y. Pei, A. LaLonde, S. Iwanaga, G. J. Snyder, *Energy Environ. Sci.* **2011**, *4*, 2085.

© 2022 The Authors. Small published by Wiley-VCH GmbH

[3] M. Samanta, T. Ghosh, R. Arora, U. V. Waghmare, K. Biswas, *J. Am. Chem. Soc.* **2019**, *141*, 19505.
[4] D. Sarkar, S. Roychowdhury, R. Arora, T. Ghosh, A. Vasdev, B. Joseph, G. Sheet, U. V. Waghmare, K. Biswas, *Angew. Chem., Int. Ed.* **2021**, *60*, 10350.
[5] Y. S. Kim, M. Brahlek, N. Bansal, E. Edrey, G. A. Kapilevich, K. Iida, M. Tanimura, Y. Horibe, S.-W. Cheong, S. Oh, *Phys. Rev. B* **2011**, *84*, 073109.
[6] S. Raoux, J. L. Jordan-Sweet, A. J. Kellock, *J. Appl. Phys.* **2008**, *103*, 114310.
[7] H.-Y. Cheng, S. Raoux, Y.-C. Chen, *J. Appl. Phys.* **2010**, *107*, 074308.
[8] S. Raoux, H.-Y. Cheng, J. L. Jordan-Sweet, B. Muñoz, M. Hitzbleck, *Appl. Phys. Lett.* **2009**, *94*, 183114.
[9] R. E. Simpson, M. Krbal, P. Fons, A. V. Kolobov, J. Tominaga, T. Uruga, H. Tanida, *Nano Lett.* **2010**, *10*, 414.
[10] R. Dingle, W. Wiegmann, C. H. Henry, *Phys. Rev. Lett.* **1974**, *33*, 827.
[11] R. Wang, W. Zhang, J. Momand, I. Ronneberger, J. E. Boschker, R. Mazzarello, B. J. Kooi, H. Riechert, M. Wuttig, R. Calarco, *NPG Asia Mater* **2017**, *9*, e396.
[12] R. Wang, D. Campi, M. Bernasconi, J. Momand, B. J. Kooi, M. A. Verheijen, M. Wuttig, R. Calarco, *Sci. Rep.* **2016**, *6*, 32895.
[13] Z. Cheng, T. Milne, P. Salter, J. S. Kim, S. Humphrey, M. Booth, H. Bhaskaran, *Sci. Adv.* **2021**, *7*, eabd7097.
[14] M. Lang, L. He, X. Kou, P. Upadhyaya, Y. Fan, H. Chu, Y. Jiang, J. H. Bardarson, W. Jiang, E. S. Choi, Y. Wang, N.-C. Yeh, J. Moore, K. L. Wang, *Nano Lett.* **2013**, *13*, 48.
[15] M. Guo, Z. Wang, Y. Xu, H. Huang, Y. Zang, C. Liu, W. Duan, Z. Gan, S.-C. Zhang, K. He, X. Ma, Q. Xue, Y. Wang, *New J. Phys.* **2016**, *18*, 015008.
[16] J. Andzane, A. Felsharuk, A. Sarakovskis, U. Malinovskis, E. Kauranens, M. Bechelany, K. A. Niherysh, I. V. Komissarov, D. Erts, *Mater. Today Energy* **2021**, *19*, 100587.
[17] Y. Jung, J. Shen, J. J. Cha, *Nano Convergence* **2014**, *1*, 18.
[18] M. Neupane, A. Richardella, J. Sánchez-Barriga, S. Xu, N. Alidoust, I. Belopolski, C. Liu, G. Bian, D. Zhang, D. Marchenko, A. Varykhalov, O. Rader, M. Leandersson, T. Balasubramanian, T.-R. Chang, H.-T. Jeng, S. Basak, H. Lin, A. Bansil, N. Samarth, M. Z. Hasan, *Nat. Commun.* **2014**, *5*, 3841.
[19] Y. Zhang, K. He, C.-Z. Chang, C.-L. Song, L.-L. Wang, X. Chen, J.-F. Jia, Z. Fang, X. Dai, W.-Y. Shan, S.-Q. Shen, Q. Niu, X.-L. Qi, S.-C. Zhang, X.-C. Ma, Q.-K. Xue, *Nat. Phys.* **2010**, *6*, 584.
[20] M. Fang, Z. Wang, H. Gu, M. Tong, B. Song, X. Xie, T. Zhou, X. Chen, H. Jiang, T. Jiang, S. Liu, *Appl. Surf. Sci.* **2020**, *509*, 144822.
[21] B. J. Kooi, M. Wuttig, *Adv. Mater.* **2020**, *32*, 1908302.
[22] I. Ronneberger, Z. Zanolli, M. Wuttig, R. Mazzarello, *Adv. Mater.* **2020**, *32*, 2001033.
[23] E. F. Steigmeier, G. Harbeke, *Solid State Commun.* **1970**, *8*, 1275.
[24] M. J. Polking, J. J. Urban, D. J. Milliron, H. Zheng, E. Chan, M. A. Caldwell, S. Raoux, C. F. Kisielowski, J. W. Ager, R. Ramesh, A. P. Alivisatos, *Nano Lett.* **2011**, *11*, 1147.
[25] X. Zhou, Y. Du, J. K. Behera, L. Wu, Z. Song, R. E. Simpson, *ACS Appl. Mater. Interfaces* **2016**, *8*, 20185.
[26] K. S. Andrikopoulos, S. N. Yannopoulos, G. A. Voyiatzis, A. V. Kolobov, M. Ribes, J. Tominaga, *J. Phys.: Condens. Matter* **2006**, *18*, 965.
[27] J. Y. Raty, V. Godlevsky, P.h. Ghosez, C. Bichara, J. P. Gaspard, J. R. Chelikowsky, *Phys. Rev. Lett.* **2000**, *85*, 1950.
[28] J.-P. Gaspard, *C. R. Phys.* **2016**, *17*, 389.
[29] J. Y. Raty, W. Zhang, J. Luckas, C. Chen, R. Mazzarello, C. Bichara, M. Wuttig, *Nat. Commun.* **2015**, *6*, 7467.
[30] A. Giussani, K. Perumal, M. Hanke, P. Rodenbach, H. Riechert, R. Calarco, *Phys. Status Solidi B* **2012**, *249*, 1939.
[31] R. Wang, J. E. Boschker, E. Bruyer, D. D. Sante, S. Picozzi, K. Perumal, A. Giussani, H. Riechert, R. Calarco, *J. Phys. Chem. C* **2014**, *118*, 29724.
[32] F. Grey, J. Bohr, *EPL* **1992**, *18*, 717.
[33] T. Nonaka, G. Ohbayashi, Y. Toriumi, Y. Mori, H. Hashimoto, *Thin Solid Films* **2000**, *370*, 258.
[34] J. Dong, F.-H. Sun, H. Tang, J. Pei, H.-L. Zhuang, H.-H. Hu, B.-P. Zhang, Y. Pan, J.-F. Li, *Energy Environ. Sci.* **2019**, *12*, 1396.
[35] L. Guarneri, S. Jakobs, A. von Hoegen, S. Maier, M. Xu, M. Zhu, S. Wahl, C. Teichrib, Y. Zhou, O. Cojocaru-Mirédin, M. Raghuwanshi, C.-F. Schön, M. Drögeler, C. Stampfer, R. P. S. M. Lobo, A. Piarristeguy, A. Pradel, J.-Y. Raty, M. Wuttig, *Adv. Mater.* **2021**, *33*, 2102356.
[36] A. V. Kolobov, M. Krbal, P. Fons, J. Tominaga, T. Uruga, *Nat. Chem.* **2011**, *3*, 311.
[37] J.-Y. Raty, M. Schumacher, P. Golub, V. L. Deringer, C. Gatti, M. Wuttig, *Adv. Mater.* **2019**, *31*, 1806280.
[38] J.-Y. Raty, M. Wuttig, *J. Phys. D: Appl. Phys.* **2020**, *53*, 234002.
[39] S. Raoux, R. M. Shelby, J. Jordan-Sweet, B. Munoz, M. Salinga, Y. C. Chen, Y. H. Shih, E. K. Lai, M. H. Lee, *Microelectron. Eng.* **2008**, *85*, 2330.
[40] S. Hasegawa, S. Ino, *Int. J. Mod. Phys. B* **1993**, *07*, 3817.
[41] P. E. Blöchl, *Phys. Rev. B* **1994**, *50*, 17953.
[42] G. Kresse, J. Furthmüller, *Phys. Rev. B* **1996**, *54*, 11169.
[43] G. Kresse, J. Furthmüller, *Comput. Mater. Sci.* **1996**, *6*, 15.
[44] G. Kresse, J. Hafner, *Phys. Rev. B* **1993**, *47*, 558.
[45] G. Kresse, D. Joubert, *Phys. Rev. B* **1999**, *59*, 1758.
[46] X. Gonze, B. Amadon, P.-M. Anglade, J.-M. Beuken, F. Bottin, P. Boulanger, F. Bruneval, D. Caliste, R. Caracas, M. Côté, T. Deutsch, L. Genovese, P.h. Ghosez, M. Giantomassi, S. Goedecker, D. R. Hamann, P. Hermet, F. Jollet, G. Jomard, S. Leroux, M. Mancini, S. Mazevet, M. J. T. Oliveira, G. Onida, Y. Pouillon, T. Rangel, G.-M. Rignanese, D. Sangalli, R. Shaltaf, M. Torrent, et al., *Comput. Phys. Commun.* **2009**, *180*, 2582.
[47] M. Torrent, F. Jollet, F. Bottin, G. Zerah, X. Gonze, *Comput. Mater. Sci.* **2008**, *42*, 337.
[48] J. P. Perdew, K. Burke, M. Ernzerhof, *Phys. Rev. Lett.* **1996**, *77*, 3865.
[49] R. F. W. Bader, M. E. Stephens, *J. Am. Chem. Soc.* **1975**, *97*, 7391.
[50] M. Yu, D. R. Trinkle, *J. Chem. Phys.* **2011**, *134*, 064111.
[51] M. Wuttig, C.-F. Schoen, M. Schumacher, J. Robertson, P. Golub, E. Bousquet, J.-Y. Raty, *Adv. Funct. Mater.* **2022**, *32*, 2110166.
[52] K. Momma, F. Izumi, *J. Appl. Cryst.* **2011**, *44*, 1272.

© 2022 The Authors. Small published by Wiley-VCH GmbH